Proton-Induced Displacement Damages in 2-D and Stacked CMOS SPADs: Study of Dark Count Rate Degradation

Ali Jouni, Mathieu Sicre, Victor Malherbe, Bastien Mamdy, Thomas Thery, Jean-Marc Belloir, Dimitri Soussan, Serge De Paoli, Vincent Lorquet, Valerian Lalucaa, et al.

Digital Object Identifier 10.1109/TNS.2023.3248521

Proton-Induced Displacement Damages in 2-D and Stacked CMOS SPADs: Study of Dark Count Rate Degradation

Ali Jouni, *Student Member, IEEE*, Mathieu Sicre, Victor Malherbe, Bastien Mamdy, Thomas Thery, Jean-Marc Belloir, Dimitri Soussan, Serge De Paoli, Vincent Lorquet, Valérian Lalucaa, Cédric Virmontois, *Senior Member, IEEE*, Gilles Gasiot, *Senior Member, IEEE*, and Vincent Goiffon, *Senior Member, IEEE*

***Abstract*— Dark count rate (DCR) degradation is measured on 40-nm 2-D and stacked CMOS single-photon avalanche diodes (SPADs) after proton irradiations. Mean DCR increase is plotted for different displacement damage doses (DDDs) for two biasing conditions. Due to field enhancement effects such as Poole–Frenkel and phonon-assisted-tunneling (PAT), non-ionizing energy loss (NIEL) scaling is found to be dependent on the excess bias. Moreover, the associated damage factors are higher compared to pixels with unity gain photodiodes. A model predicting DCR increase with DDD based on field enhancement factor equations and damage energy deposited by the proton-induced recoil spectrum is established and fits well with experimental data. Finally, activation energies are extracted: low values between 25 °C and 60 °C confirm the domination of field effects over thermal generation. Furthermore, large energy discrepancies seen at a fixed DCR increase are suggesting that defect structures could also have an impact on DCR distributions.**

***Index Terms*— CMOS, dark count rate (DCR), displacement damage dose (DDD), non-ionizing energy loss (NIEL), proton, radiation, single-photon avalanche diode (SPAD), stacking, thermal activation energy.**

I. Introduction

SINGLE photon sensitivity and high timing resolution abilities, achievable with single-photon avalanche diodes (SPADs), have found several applications for space missions, such as time-of-flight (ToF) and 3-D imaging using LiDARs or Gamma detection with a scintillating fiber [1]. Moreover, the NewSpace trend has broadened the accessibility to space for industrials and university laboratory, implying lower mission costs and the use of commercial-off-the-shelf (COTS) CMOS devices [2]. They bring the advantage of large array integration coupled to advanced technology nodes. It also allows active quenching circuit (AQS) integration that reduces SPAD dead time to tenth of nanoseconds. Finally, efforts have been made toward higher fill factor (FF) with stacking techniques [3]. However, COTS SPADs sometimes suffer from lower performances [4] and a weaker radiation hardness than custom processes. Therefore, it is important to predict and quantify the effect of a space radiation environment on that kind of device by means of particle irradiation tests.

Numerous studies related to radiation damages on 2-D SPADs exist, from total ionizing dose (TID) effects with X-ray irradiations [5] to displacement damage dose (DDD) effects with alpha particles, neutrons [5], [6] or protons [7]. For all types of incident particles, the main parameter monitored is the dark count rate (DCR) degradation before, during, and after irradiation. While TID induces small DCR changes [5] thanks to optimal isolation of the depletion volume from shallow trench isolation (STI) in CMOS technology, DDD-induced bulk damages (mainly clusters of defects for neutrons and high energy protons; mainly point defects for low-energy protons and alpha particles) increase the DCR by one to several decades, leading to out-of-specification devices. In some cases [6], [8], DCR can exhibit random telegraph signal (RTS) behavior that could be explained by the presence of defect clusters with metastable configurations [9]. However, origins and characteristics of RTS are still under study.

In this work, proton irradiations were performed on silicon based 2-D SPAD arrays and R&D stacked SPADs using a 62-MeV proton beam. Fluences between 2.0×10^{10} and 1.6×10^{11} p/cm^2 were reached. Unlike previous work, the effect of excess bias during irradiation for 2-D SPADs is studied. An analytical model is established to predict the DCR increase with the DDD. Moreover, activation energy distributions are presented and allow us to link a specific DCR increase to a main carrier generation mechanism. Finally, first insight into the behavior of SPADs implemented in stacking structures to proton irradiations are given.

II. Experimental Description

A. Device Description

2-D and stacked SPADs manufactured in a 40-nm CMOS technology were irradiated with protons. 2-D samples consist

This work was supported in part by CNES, in part by STMicroelectronics, and in part by ISAE-SUPAERO.

Ali Jouni, Jean-Marc Belloir, Valérian Lalucaa, and Cédric Virmontois are with CNES, 31400 Toulouse, France (e-mail: ali.jouni@isae-supaero.fr).

Mathieu Sicre, Victor Malherbe, Bastien Mamdy, Thomas Thery, Dimitri Soussan, Serge De Paoli, Vincent Lorquet, and Gilles Gasiot are with STMicroelectronics, 38920 Crolles, France.

Vincent Goiffon is with Département Electronique Optronique et Signal (DEOS) ISAE-SUPAERO, 31400 Toulouse, France.

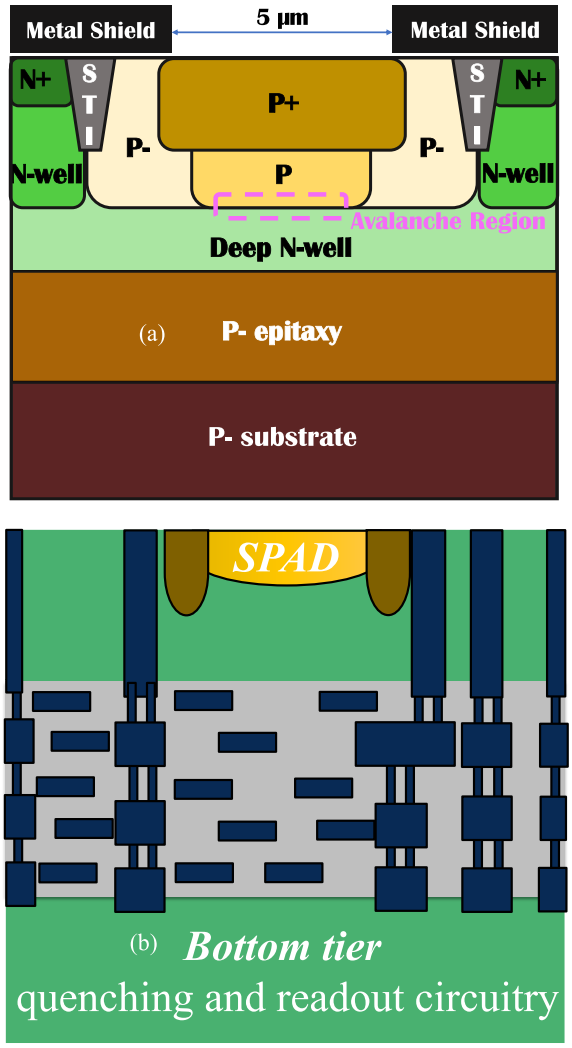

Fig. 1. (a) Schematic cross section of the 2-D SPAD used in this work. (b) Stacking structure.

of 30 × 30 squared SPADs with a 5 × 5 μm^2 active area. The pixel pitch is 7.8 μm. A cross section of the diode is given in Fig. 1(a). An integrated quenching transistor stops the avalanche and then resets the SPAD. Next, a NAND function senses the voltage drop across the photodiode and a counter scores the number of triggering events N_e during the integration time τ_i. The number of counts per second (cps) is thus deduced by dividing N_e by τ_i (in seconds). We took $\tau_i = 1$ s to have a good DCR estimation for low DCR pixels (less than 100 cps). These devices have a breakdown voltage around $V_{\text{BD}} = 14$ V. More details about 2-D SPAD performances and pixel circuitry are given in [6] and [10].

R&D stacked chips studied in this article embedded four SPADs implemented on a top layer bounded to another one containing the pixel circuitry. A total of 32 stacked SPADs were irradiated. There is also a passive quenching stopping the impact ionization process with an inverter sensing the voltage pulse. This passive circuitry is different from the 2-D SPAD one. The advantages brought by these structures

TABLE I
DETAILED DESIGN OF EXPERIMENTS

Device	#	Bias (V)	Proton Energy (MeV)	Fluence (p/cm^2)	DDD (TeV/g)
2D_SPAD1	1	$V_{HV0}+1$	56	2.0×10^{10}	84.7
2D_SPAD2	1	$V_{HV0}+3$	56	2.0×10^{10}	84.7
2D_SPAD3	1	0	62	8.0×10^{10}	316
R&D_SPAD1	4	0	62	8.0×10^{10}	316
R&D_SPAD2	4	0	62	1.6×11^{11}	632

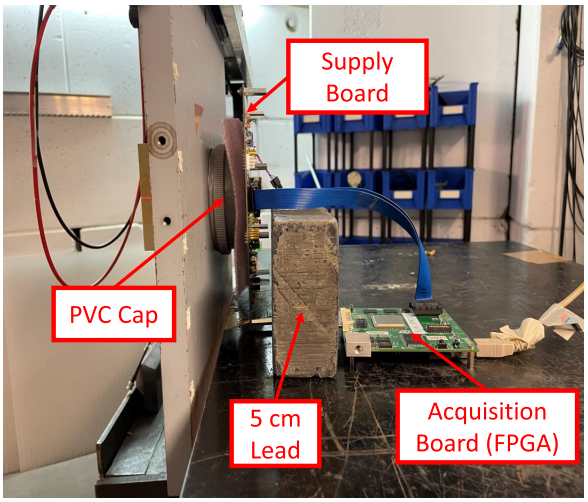

Fig. 2. Setup for 2-D SPAD active irradiations.

are an improved FF, the integration of more functionalities and the possibility to manufacture larger arrays with layout optimization [11]. The stacking technique is presented in Fig. 1(b).

B. Irradiation Setup

The 62-MeV proton beam was used at Université Catholique de Louvain (UCL) in Belgium. Table I summarizes the design of experiments. Two samples were irradiated actively (meaning that a bias was applied during irradiations): V_{HV0} represents the addition of the breakdown voltage with the CMOS logic level (0.6 V) required by the NAND gate to sense a pulse. The maximum TID (SiO_2) reached by these irradiations, calculated using SRIM tool for linear energy transfer (LET) estimations, is less than 35 krad (SiO_2). It is well known that CMOS SPADs are not sensitive to TID up to the Mrad (SiO_2) range [6]: it can thus be assumed that ionizing effects are negligible and only the DDD affects the SPAD behavior. The setup used for active irradiations on 2-D SPADs is presented in Fig. 2: chips are supplied by a first board connected to an FPGA, allowing communications between SPADs and a computer located outside the radiation chamber. Dark conditions for DCR measurements during irradiations are ensured by screwing a 5-mm rigid polyvinyl

chloride (PVC) to the supply board. It decreases the energy of the protons impacting the SPAD sensitive area to 56 MeV (calculated using SRIM tool). Finally, passive irradiations (bias voltage = 0 V) were also performed.

III. DCR Increase Model and Irradiation Results

A. DCR Increase Model

The purpose of the model is to predict the mean DCR increase at different proton doses. It is based on the convolution of SPAD electrical properties (extracted from electric field profile data) with the distribution of the effective damage energy deposited in the depletion region. In fact, for CMOS image sensor pixels (CIS), with electric fields below 10^5 V/cm, non-ionizing energy loss (NIEL) scaling phenomena has been verified [11] and can relate a damage at the atomic level after a particle collision to a specific dark current increase ΔDC in electrons per second ($e-$/s) [12]

$$\Delta \mathrm{DC}[e^-/\mathrm{s}] = K_D \times \frac{E_D}{\rho_{\mathrm{Si}}} \tag{1}$$

with K_D the universal damage factor, E_D the effective deposited damage energy converted into displaced Si atoms, and ρ_{Si} the silicon density. In the case of SPADs, the DCR increase ΔDCR is measured in avalanches or cps. However, a generated electron-hole pair has a certain probability P_{TOT} of triggering avalanches, which must be considered for the computation of ΔDCR. Furthermore, inside the SPAD depletion region, the electric field strength is greater than 10^5 V/cm.: an electric field-enhanced carrier generation by a factor EF compared to low field regime will thus impact the DCR increase. Thereby, ΔDCR can be retrieve based on (1) by

$$\Delta \mathrm{DC}[e^-/\mathrm{s}] = \mathrm{EF} \times P_{\mathrm{TOT}} \times K_D \times \frac{E_D}{\rho_{\mathrm{Si}}}. \tag{2}$$

Therefore, we need to determine P_{TOT} and EF with the electric field data for a fixed biasing condition on one hand, and on the other hand simulate the distribution of E_D. As the model will be tested only for active irradiations, we use a proton energy of 56 MeV. Moreover, electric fields and proton damages will be considered only in SPAD space charge regions (SCRs). This is justified by the lower impact of areas outside the depletion region due to lower electric fields.

First, the recoil energy spectrum induced by 56-MeV protons is estimated with the use of the GEANT 4 algorithm. Nuclear elastic, nonelastic, and inelastic collisions are considered. Then, this spectrum is injected into the TIARA code [13]. This algorithm can simulate each SPAD layer (from metals to the silicon substrate) and introduces proton interactions based on GEANT 4 database. Positions of collisions between protons and first Si atoms are uniformly distributed throughout the SCR. In fact, for 56-MeV protons, the energy loss after crossing the depletion region is less than 1 MeV and can be neglected. Each recoil is then followed, and the deposited damage energy is computed along the trajectory by considering the electronic loss (Lindhard partition). The TIARA output gives the distribution of the deposited energy E_D^* in the SCR. Nevertheless, this value is overestimated compared to the energy effectively converted into displaced atoms. It is due to numerous interactions depositing damage energies which are below the threshold leading to a removal of a Si atoms (between 15 and 21 eV [14]). We take this into account by using TRIM tools that output the effective damage energy E_D deposited in the SCR giving rise to displacement damages.

Second, the electric field F inside the SCR is simulated using TCAD tools for fixed biasing conditions. First, these data are used to determine the ionization coefficients $\alpha_{e,h}$ for electrons and holes. For each carrier, theses quantities represent the number of electron-hole pairs created by impact ionization per unit length. We use the van Overstraeten - de Man model [15] which predicts an exponential evolution of α_e and α_h (Chynoweth law [16])

$$\alpha_{e,h}(z) = \gamma \times a_{e,h} \times \exp\left(-\frac{\gamma . b_{e,h}}{F(z)}\right) \tag{3}$$

where z is the axis perpendicular to the junction and γ a temperature dependent coefficient associated with phonons interacting with charge carriers. $a_{e,h}$ and $b_{e,h}$ are normalization parameters depending on the type of carrier and the electric field strength. Theses ionization coefficients are then injected into the differential equations coupling the probability for an electron or a hole $P_{e,h}$ to trigger an avalanche after drifting from the position z to the end of the avalanche zone [17]

$$\begin{cases} \dfrac{dP_e}{dz} = -(1-P_e) \times \alpha_e \times (P_e + P_h - P_e \times P_h) \\ \dfrac{dP_h}{dz} = (1-P_h) \times \alpha_h \times (P_e + P_h - P_e \times P_h) \end{cases} \tag{4}$$

considering $z = 0$ the p-doped side of the junction. The total breakdown probability $P_{\mathrm{TOT}}(z)$ is then deduced

$$P_{\mathrm{TOT}}(z) = P_e(z) + P_h(z) - P_e(z) \times P_h(z). \tag{5}$$

Finally, the enhancement factor EF is calculated by considering two high field effects: the Poole–Frenkel effect and the phonon-assisted tunneling (PAT). In our model, we will only consider the emission of an electron from a trap level to the conduction band. The Poole–Frenkel effect corresponds to the lowering of the barrier that an electron located in a trap must overcome to be in the conduction band. Then, PAT is the combination of electron thermal excitation (via phonons) and the tunneling effect through the barrier. It is thus coupled with the barrier lowering of the Poole–Frenkel effect. These two field effects are summarized in Fig. 3. We use the 3-D-coulombic well potential for the conduction band deformation introduced by a defect. Vincent et al. [18] and Martin et al. [19] give analytical solutions for the contribution

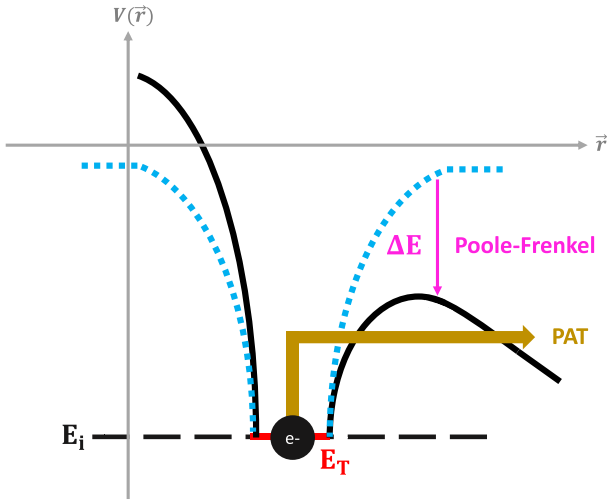

Fig. 3. Two field enhancement effects: the barrier lowering (Poole–Frenkel, pink) and the PAT (gold).

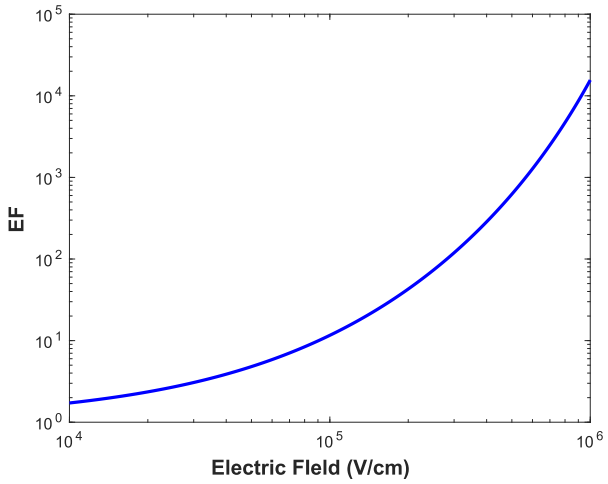

Fig. 4. Total enhancement factor for a 3-D-coulombic well model for band deformations.

to the total enhancement factor for both effects

$$\mathrm{EF_{PF}} = \frac{1}{2} + \frac{1 + \left(\frac{\Delta E}{k_B.T} - 1\right) \times \exp\left(\frac{\Delta E}{k_B.T}\right)}{\left(\frac{\Delta E}{k_B.T}\right)^2} \tag{6}$$

$$\begin{aligned}\mathrm{EF_{PAT}} = 2 \times \pi \\ \times \int_{\frac{\Delta E(\theta)}{k_B.T}}^{\frac{E_C - E_T}{k_B.T}} \left[\int_0^{\frac{\pi}{2}} \exp\left(z' - z'^{3/2} \right.\right. \\ \left. \times \left(\frac{4.(2.m^*)^{1/2}.(k_B.T)^{3/2}}{3.\hbar.F(z)} \right) \right. \\ \left. \left. \times \left(1 - \left(\frac{\Delta E(\theta)}{z.k_B.T} \right)^{5/3} \right) \right) dz' \right] \\ \times \sin(\theta)\, d\theta \end{aligned} \tag{7}$$

with k_B the Boltzmann's constant, T the temperature, E_C the conduction band energy, E_T the trap energy, m^* the effective mass of carriers, $\hbar$ the reduced Planck constant, and F the local electric field. $\Delta E(\theta)$ is the barrier lowering depending on the angle θ between the charge emission direction and the electric field

$$\Delta E(\theta) = \left(\frac{q^3 \cdot F \cdot \cos(\theta)}{\pi \cdot \epsilon} \right)^{1/2} \tag{8}$$

with ϵ the silicon permittivity. ΔE in (6) and (7) corresponds to $\Delta E(0)$. We plot in Fig. 4 the expected total enhancement factor EF (corresponding to $\mathrm{EF_{PF}} + \mathrm{EF_{PAT}}$). Electric fields outside the SCR tend to 10^4 V/cm, meaning that EF is around 1. Therefore, it can be neglected compared to EF computed in the SCR, where electric fields tends to 5×10^5 V/cm. Our assumption made above of considering only proton damages occurring in the depletion region is thus confirmed. Finally, a Monte-Carlo algorithm is run to predict the DCR increase using (2) for a given proton fluence. Indeed, the use of GEANT 4 and TIARA code allow us to deduce the number λ of proton-Si collisions leading to a damage energy deposition inside the SCR for any fluence. We assume a Poisson distribution with a parameter λ for each pixel. Then, as the collision probability inside the SCR was supposed to be uniform over this region, a collision position following a uniform distribution is simulated. This allows us to compute the local value of P_{TOT} and EF. Finally, we draw a deposited damage energy E_D following the distribution outputted by GEANT4, TIARA, and TRIM. At this stage, the theoretical DCR increase $\Delta\mathrm{DCR_{theo}}$ can be computed. However, it must be compared to the experimental one $\Delta\mathrm{DCR_{exp}}$ by removing the contribution of coulombic nuclear interactions which are not modeled here. According to [20] and [21], coulombic interactions for protons contribute one third of their total NIEL. Therefore, $\Delta\mathrm{DCR_{theo}}$ must be compared to $0.67 \times \Delta\mathrm{DCR_{exp}}$.

B. NIEL Scaling and Damage Factors

One of the advantages brought by active irradiations is that the mean DCR increase can be measured with time, or equivalently with DDD, and NIEL scaling can be verified. These two last quantities can be introduced in (2) by

$$\begin{aligned} 2\Delta\mathrm{DCR} &= P_{\mathrm{TOT}} \times \mathrm{EF} \times K_D \times V_D \times \Psi \times \mathrm{NIEL} \\ &= P_{\mathrm{TOT}} \times \mathrm{EF} \times K_D \times V_D \times \mathrm{DDD} \end{aligned} \tag{9}$$

with Ψ the proton fluence in p/cm^2, V_D the depletion region volume in cm^3, NIEL in MeV $\cdot$ cm^2 $\cdot$ g^{-1} depending on particle type and energy, and DDD in MeV $\cdot$ g^{-1}. We can also define a pseudo damage factor K_D^*

$$K_D^* = \overline{P_{\mathrm{TOT}}} \times \overline{\mathrm{EF}} \times K_D \tag{10}$$

with $\overline{P_{\mathrm{TOT}}}$ and $\overline{\mathrm{EF}}$ the integration of P_{TOT} and EF over the depletion region. In Fig. 5, we plot the mean DCR increase against DDD for both active irradiations made at different excess biases. Gap between first points and their respective linear fit is due to low statistics. In fact, only few pixels were hit after first acquisitions, but the mean DCR increase is measured across the whole matrix. Therefore, depending on

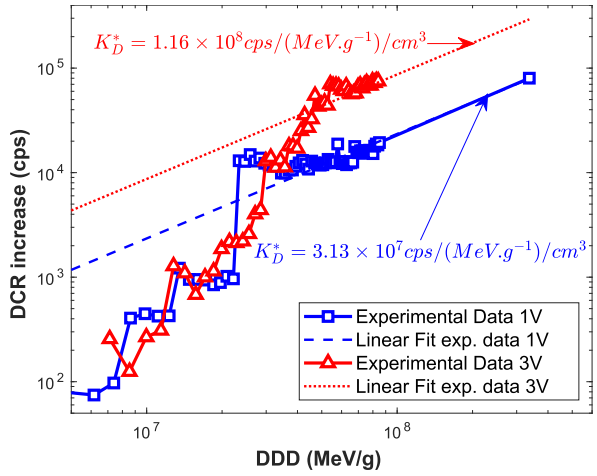

Fig. 5. DCR increase measured for different DDD (active irradiations).

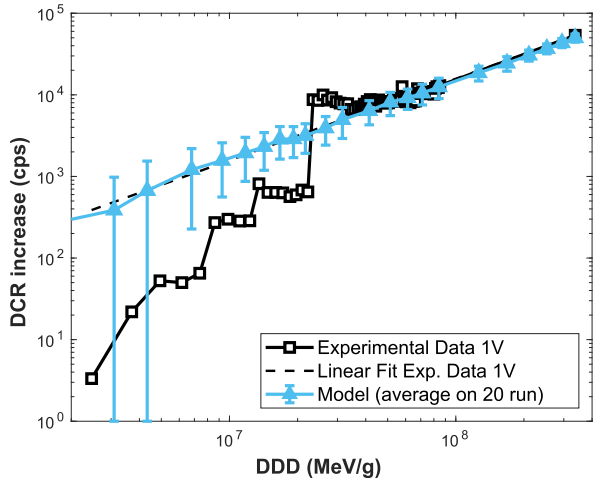

Fig. 6. Comparison between experimental data and our model at 1 V above V_{HV0}.

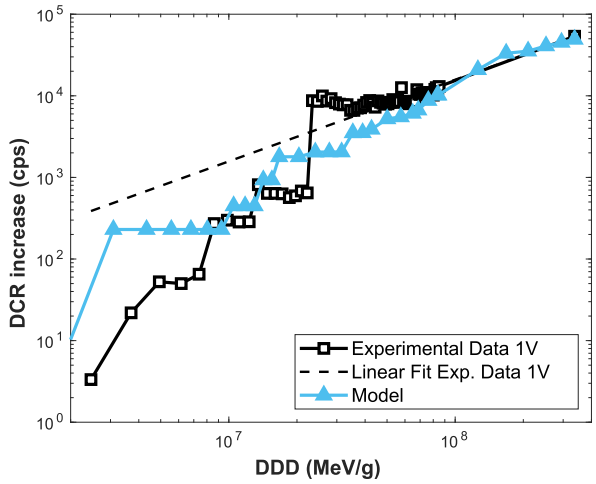

Fig. 7. Comparison between experimental data and our model at 1 V above V_{HV0} for only one run of the model. Statistical behaviors (steps in DCR increase) are also observed in the model.

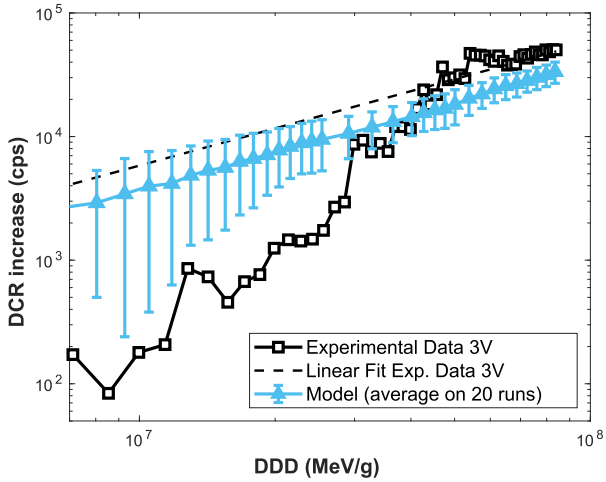

Fig. 8. Comparison between experimental data and our model at 3 V above V_{HV0}.

where the proton collided in the SCR and on the associated deposited energy E_D, first points will be at different DCR increases from one irradiation to another. To confirm this statement, we expect large standard deviations for low DDD points with our model but a linear trend if we average the model over several runs.

The best linear fits have also been extracted in Fig. 5 for both active irradiations to evaluate K_D^*. As expected with the fast increase of EF with the electric field and thus the excess bias, K_D^* is higher for 3 V above V_{HV0}. Moreover, both factors are consistent with [6] where K_D^* is found to be equal to $(7 \pm 2) \times 10^7$ cps/(MeV $\cdot$ g^{-1})/cm^3 on the same chips irradiated at 1.3-V excess bias with a large neutron spectrum. In conventional photodiodes where electric field magnitudes are below the threshold of 10^5 V/cm, pure Shockley-Read-Hall (SRH) thermal generation is usually found. In this case, the induced defects are independent of the voltage applied, implying a universal damage factor K_D that is also independent of doping profiles.

In Fig. 6, our model is compared to experimental data at 1-V excess bias. The model was run 20 times, and the average DCR increase for different DDD are computed. Standard deviations are taken for each point to draw the error bars. We see that our model fits very well with experimental data. As mentioned before and verified with simulations, we see a large spread around the mean for first points due to a very low number of events per SPADs (<0.01) for 900 pixels. This can be verified in Fig. 7, where the model was run only once: we notice the same steps in DCR increase as seen in the experimental data. In this simulation, low DDD points are also under the linear fit.

Finally, we can also observe in Fig. 8 good results between our model and the 3-V data. In this case, the model is a bit underestimated compared to the fit, but some reasons can be underlined: first the active irradiation was performed only once. Thereby and as discussed before, discrepancies exist for each data point, leading to uncertainties for the linear fit. Moreover, at this excess bias, the gradient of the electric field is very strong. This tends to weaken our approach of computing the breakdown probability P_{TOT}. Indeed, charge

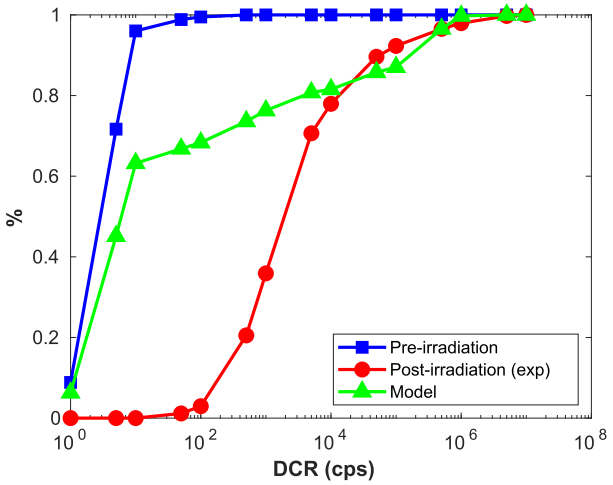

Fig. 9. DCR cumulative histogram before and three weeks after passive irradiation at a fluence of 8.0×10^{10} p/cm^2. The histogram simulated with our model is also present.

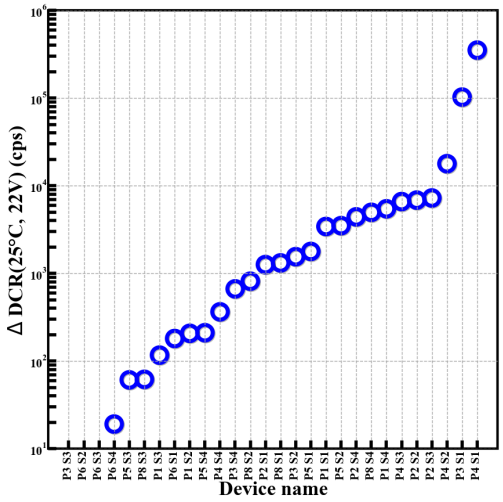

Fig. 10. Normalized DCR increase measured on passively irradiated stacked SPAD up to 1.6×10^{11} p/cm^2 (three weeks after irradiations). Results for only 25 stacked SPADs over the 32 irradiated are plotted in the x-axis.

carriers travel a distance, the dead space, before having enough energy to ionize along their path [22]. If the electric field gradient is too high, there will be a delay (in the picosecond scale) before the charge carrier gains or loses energy. This dead space is not considered in our model, and the higher the bias voltage, the higher the electric field gradient.

C. DCR Distributions

Fig. 9 displays DCR pre- and post-irradiation cumulative histograms using the data measured on the passively irradiated 2-D SPAD array at 8.0×10^{10} p/cm^2. DCR is measured at 1-V excess bias. We also simulate a DCR distribution with our model. First, the experimental histogram shows a large distribution of the DCR. In fact, 60% of the SPADs have a DCR between 10^3 and 10^7 cps. We can also note that our model does not reproduce the experimental data below 5×10^3 cps but fits well above. This is due to the crosstalk near the hottest pixels [23]. For the 2-D SPADs used in this study, this parameter is estimated at 1%. For example, it means that a DCR of 10^4 cps is added at the vicinity of a pixel at 10^6 cps. In the best case, it was thus expected that our model would only fit the upper part of the histogram. Crosstalk also explains why the experimental curve is near 0% for DCR below 100 cps.

Data for stacked SPADs are displayed in Fig. 10. As for 2-D SPADs, we see a large variety of DCR increase induced by proton impacts. For both SPAD structures, this spread in DCR is due to the correlation of two parameters. The first one is the complexity of defects, with the formation of small or large clusters that will act as generation centers of carriers [9]. In the same conditions (temperature and electric field), a bigger cluster is likely to have a greater carrier generation rate and will thus bring a higher DCR increase. There is also a dependence on the induced trap energy inside the band gap. According to SRH theory, the more this energy is close to mid-gap, the higher the associated generation rate will be. Finally, the second parameter is the position of the defect inside the depletion region. A generation center located inside the SCR but near the edge will induce a lower DCR increase than the same defect located at the center of the depletion region at fixed temperature. In fact, the higher electric field of the SCR center will induce a higher amplification of the number of dark counts through Poole–Frenkel effect and PAT than at the edge where the electric field is weaker. If the defect is located outside the SCR, the induce DCR will also be weaker because only thermal effects will dominate (diffusion current). At room temperature, at which irradiations were performed, electric field effects induce a higher DCR degradation than thermal effect for the same defect. Finally, as discussed in the description of our model, P_{TOT} and EF depend on the local electric field strength.

D. Activation Energies Measured on 2-D and Stacked SPADs

In this paragraph, we focus on activation energies of proton-induced defects. For pure thermal generation of electrons or holes, this parameter links the generation rate of free carriers (and thus the DCR of SPADs) with temperature according to

$$U_{\mathrm{SRH}} \propto \mathrm{DCR} \propto \exp\left(-\frac{E_a}{k_B.T}\right) \tag{11}$$

with U_{SRH} the SRH generation rate of the defect in $e-/\mathrm{s}$ and E_a its activation energy in eV. The lowest expected E_a is related to mid-gap defects, with an experimental value of 0.63 eV for these defects [21]. However, when field effects are at play, E_a is lowered [24]. Estimations using (6) and (7) show that a lowering of several tenths of eV is expected for SPADs.

In Fig. 11 mean activation energies before and after irradiation for the 2-D SPAD array irradiated at 8.0×10^{10} p/cm^2 are plotted. E_a are extracted between 25 °C and 45 °C and are displayed for different excess biases V_{ex}. We see a general trend, with defect activation energy decreasing for high DCR

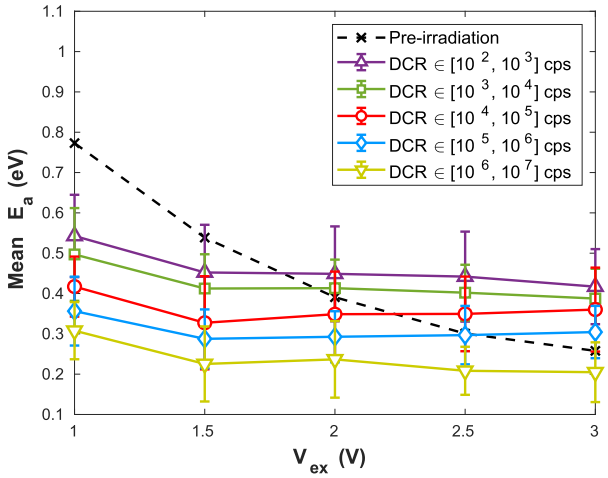

Fig. 11. Mean activation energies at different excess biases for different groups of DCR measured on the passively irradiated SPADs (8.0×10^{10} p/cm^2).

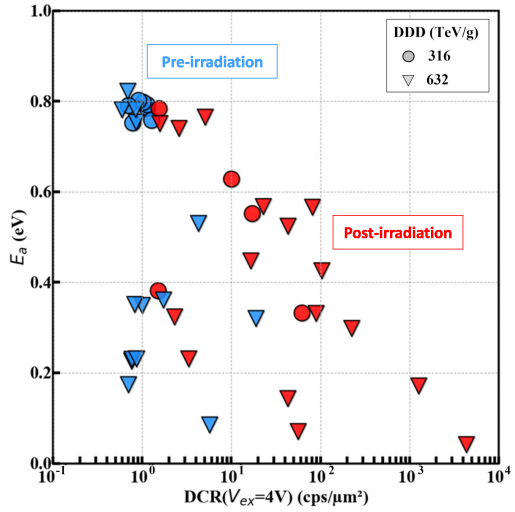

Fig. 12. Activation energies at fixed excess bias for all the stacked SPADs irradiated.

groups. As mentioned above, values below 0.63 eV for any V_{ex} underline electric field enhancement effects. Furthermore, large spreads around mean activation energies for each DCR group highlight the variety of defects related to a particular DCR. This is linked with our explanation of DCR cumulative histograms, with the correlation of defect structures with the position inside the device. Indeed, a large cluster of defects due to a high energy deposition E_D formed at the edge of the SCR can induce the same DCR increase than a smaller one located in the center of the avalanche zone due to the exponential dependence of EF. However, the smaller cluster will have a lower activation energy.

Activation energies extracted between 25 °C and 60 °C for stacked SPADs are displayed in Fig. 12 with a similar behavior in terms of E_a values and their dependencies with the DCR induced by proton defects. In fact, we retrieve the trend of lower E_a when SPAD DCRs are increasing. Higher values of activation energy compared to 2-D SPADs for some pixels with DCR below 100 cps is due to the temperature range in which E_a is extracted. Between 45 °C and 60 °C, thermal generation in the SCR and diffusion from outside the depletion region start to be significant. Therefore, E_a is increased.

IV. Conclusion

Proton irradiations on 40-nm 2-D and R&D stacked SPADs are studied in this article for different fluences and different biasing conditions. Through active irradiations, NIEL scaling has been observed for 1- and 3-V excess bias on 2-D arrays. We have established a Monte Carlo model based on the computation of the breakdown probability, the field enhancement factor, and the deposited damage energy distribution after proton-Si collisions. We saw that this model fits very well with experimental data. Low activation energies were extracted from irradiated 2-D and stacked SPADs. The same trend of a decreasing E_a for higher DCR was noticed and expected from our model that suggested a higher activation energy lowering where the electric is higher, or equivalently where the enhancement factor is higher. Furthermore, E_a distributions and cumulative histograms have shown the variety of these defects that is due to the correlation of defect structures and their positions inside the depletion region.

Acknowledgment

The authors would like to thank Université Catholique de Louvain (UCL) for the use of the proton beam line and their assistance during irradiations.

References

[1] M. Marisaldi et al., "Single photon avalanche diodes for space applications," in *Proc. IEEE Nucl. Sci. Symp. Conf. Rec.*, Anaheim, CA, USA, Oct. 2012, pp. 129–134.

[2] P. Jerram and K. Stefanov, "CMOS and CCD image sensors for space applications," in *High Performance Silicon Imaging*, 2nd ed. Amsterdam, The Netherlands: Elsevier, 2020, ch. 9, sec. 9.5, pp. 273–283.

[3] E. Charbon, C. Bruschini, and M.-J. Lee, "3D-stacked CMOS SPAD image sensors: Technology and applications," in *Proc. 25th IEEE Int. Conf. Electron., Circuits Syst. (ICECS)*, Bordeaux, France, Dec. 2018, pp. 1–4.

[4] D. Bronzi, F. Villa, S. Tisa, A. Tosi, and F. Zappa, "SPAD figures of merit for photon-counting, photon-timing, and imaging applications: A review," *IEEE Sensors J.*, vol. 16, no. 1, pp. 3–12, Jan. 2016.

[5] L. Ratti et al., "Dark count rate degradation in CMOS SPADs exposed to X-rays and neutrons," *IEEE Trans. Nucl. Sci.*, vol. 66, no. 2, pp. 567–574, Feb. 2019.

[6] V. Malherbe, S. De Paoli, B. Mamdy, G. Gasiot, and P. Roche, "Displacement damage characterization of CMOS single-photon avalanche diodes: Alpha-particle and fast-neutron measurements," *IEEE Trans. Nucl. Sci.*, vol. 68, no. 5, pp. 777–784, May 2021.

[7] M. Campajola, F. Di Capua, D. Fiore, C. Nappi, E. Sarnelli, and L. Gasparini, "Long-term degradation study of CMOS SPADs in space radiation environment," in *Proc. 18th Eur. Conf. Radiat. Effects Compon. Syst. (RADECS)*, Gothenburg, Sweeden, Sep. 2018, pp. 87–91.

[8] F. Di Capua et al., "Random telegraph signal in proton irradiated single-photon avalanche diodes," *IEEE Trans. Nucl. Sci.*, vol. 65, no. 8, pp. 1654–1660, Aug. 2018.

[9] A. Jay et al., "Simulation of single particle displacement damage in silicon—Part II: Generation and long-time relaxation of damage structure," *IEEE Trans. Nucl. Sci.*, vol. 64, no. 1, pp. 141–148, Jan. 2017.

[10] S. Pellegrini et al., "Industrialised SPAD in 40 nm technology," in *IEDM Tech. Dig.*, San Francisco, CA, USA, Dec. 2017, p. 16.

[11] J. R. Srour and D. H. Lo, "Universal damage factor for radiation-induced dark current in silicon devices," *IEEE Trans. Nucl. Sci.*, vol. 47, no. 6, pp. 2451–2459, Dec. 2000.

[12] C. Virmontois et al., "Displacement damage effects due to neutron and proton irradiations on CMOS image sensors manufactured in deep submicron technology," *IEEE Trans. Nucl. Sci.*, vol. 57, no. 6, pp. 3101–3108, Dec. 2010.

[13] T. Thery, G. Gasiot, V. Malherbe, J.-L. Autran, and P. Roche, "TIARA: Industrial platform for Monte Carlo single-event simulations in planar bulk, FD-SOI, and FinFET," *IEEE Trans. Nucl. Sci.*, vol. 68, no. 5, pp. 603–610, May 2021.

[14] I. Santos, L. A. Marqués, and L. Pelaz, "Modeling of damage generation mechanisms in silicon at energies below the displacement threshold," *Phys. Rev. B, Condens. Matter*, vol. 74, no. 17, Nov. 2006, Art. no. 174115.

[15] R. Van Overstraeten and H. De Man, "Measurements of the ionization rates in diffused silicon p-n junctions," *Solid-State Electron.*, vol. 13, no. 1, pp. 583–608, May 1970.

[16] A. G. Chynoweth, "Ionization rates for electrons and holes in silicon," *Phys. Rev.*, vol. 109, no. 5, pp. 1537–1540, Mar. 1958.

[17] W. G. Oldham, R. R. Samuelson, and P. Antognetti, "Triggering phenomena in avalanche diodes," *IEEE Trans. Electron Devices*, vol. ED-19, no. 9, pp. 1056–1060, Sep. 1972.

[18] G. Vincent, A. Chantre, and D. Bois, "Electric field effect on the thermal emission of traps in semiconductor junctions," *J. Appl. Phys.*, vol. 50, no. 8, pp. 5484–5487, Aug. 1979.

[19] P. A. Martin, B. G. Streetman, and K. Hess, "Electric field enhanced emission from non-Coulombic traps in semiconductors," *J. Appl. Phys.*, vol. 52, no. 12, pp. 7409–7415, 1981.

[20] I. Jun et al., "Proton nonionizing energy loss (NIEL) for device applications," *IEEE Trans. Nuc. Sci.*, vol. 50, no. 6, pp. 1924–1927, Dec. 2003.

[21] J. M. Belloir, "Spectroscopie du courant d'obscurité induit par les effets de déplacement atomique des radiations spatiales et nucléaires dans les capteurs d'images CMOS à photodiode pincée," Ph.D. dissertation, Dept. Electronique Optronique et Signal (DEOS), Univ. Toulouse, Toulouse, France, 2016.

[22] A. Spinelli, A. Pacelli, and A. L. Lacaita, "Dead space approximation for impact ionization in silicon," *Appl. Phys. Lett.*, vol. 69, no. 24, pp. 3707–3709, Dec. 1996.

[23] J. A. Smith et al., "Evaluation of an operational concept for improving radiation tolerance of single-photon avalanche diode (SPAD) arrays," *IEEE Trans. Nucl. Sci.*, vol. 67, no. 5, pp. 797–804, May 2020.

[24] J. R. Srour and R. A. Hartmann, "Enhanced displacement damage effectiveness in irradiated silicon devices," *IEEE Trans. Nucl. Sci.*, vol. 36, no. 6, pp. 1825–1830, Dec. 1989.